THE JOURNAL OF PHYSICAL CHEMISTRY C
A JOURNAL OF THE AMERICAN CHEMICAL SOCIETY

pubs.acs.org/JPCC
Article

Co-sintering Reaction Analysis of $LiCoO_2$ Cathodes and NASICON-Type LATP Solid Electrolytes Studied by Experimental and Computational Methods

Fumihiko Ichihara, Shogo Miyoshi, Machiko Ode, and Takuya Masuda*

Cite This: *J. Phys. Chem. C* 2025, 129, 12738−12749
Read Online

ACCESS | Metrics & More | Article Recommendations | Supporting Information

ABSTRACT: $LiCoO_2$ (LCO), a practical cathode material for Li-ion batteries, and $Li_{1.3}Al_{0.3}Ti_{1.7}(PO_4)_3$ (LATP), an oxide-based solid electrolyte, were mixed at different ratios and cosintered at various temperatures. The reaction products in the crystalline and amorphous phases formed during sintering were quantitatively analyzed by X-ray diffraction (XRD) and X-ray absorption near edge structure (XANES). LCO and LATP reacted with each other to form Co_3O_4, Li_3PO_4, and amorphous-TiO_2 in either mixing ratios when sintering at relatively low temperatures (<500 °C). At the sintering temperatures between 500 and 900 °C, $LiCoPO_4$, $CoTiO_3$, and rutile-TiO_2 were formed for LCO and LATP at a volume ratio of 3:7; Co_2TiO_4, $CoTiO_3$, and Co_3O_4 at a volume ratio of 5:5; and Li_2TiO_3, Co_2TiO_4, and Co_3O_4 at a volume ratio of 7:3. We conducted thermodynamic calculations of the same system at various temperatures under an oxygen partial pressure of 0.21 atm to compare with actual reaction products determined by XRD and XANES. At 900 °C, the experimentally observed actual reaction products were reasonably reproduced by the thermodynamic calculations except for a few discrepancies. The discrepancies between the identified reaction products and the predicted thermodynamically stable phases were attributed to (1) the formation of alternative phases that have Gibbs free energies comparable to the predicted most stable phases and (2) the occurrence of phase transformation of high temperature phases during the cooling process to perform product analysis at room temperature. Meanwhile, as the temperature became lower from 900 °C, discrepancies between experimental results and calculations became more prominent, so that the starting materials and reaction products increased and decreased, respectively, probably due to the slow kinetic process such as mutual diffusion as evidenced by elongating the sintering time and using smaller grain sizes.

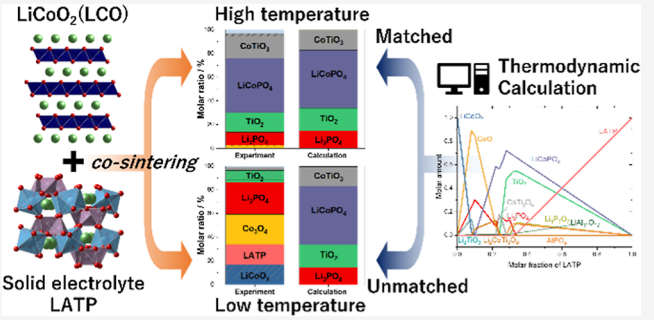

INTRODUCTION

Lithium-ion batteries (LIBs) have been used in a wide range of applications including electric vehicles, portable devices, and energy storage systems due to their high energy density and durability.[1−3] Since conventional LIBs using a flammable organic electrolyte have safety concerns, the development of safer and more reliable rechargeable batteries is strongly desired. All solid-state LIBs (ASSLIBs) especially using a nonflammable and thermodynamically stable oxide-based solid electrolyte are promising candidates because of their extremely high safety and potentially long cycle life.[3−5] Among various oxide-based solid electrolytes, NASICON-type $Li_{1.3}Al_{0.3}Ti_{1.7}(PO_4)_3$ (LATP),[6,7] perovskite-type $Li_{0.29}La_{0.57}TiO_3$ (LLTO),[8,9] and garnet-type $Li_7La_3Zr_2O_{12}$ (LLZO)[10,11] attract much attention due to their superior lithium-ion conductivities. However, unlike conventional liquid-type LIBs in which electrode/electrolyte interfaces can be spontaneously formed by injecting an organic electrolyte solution, the formation of a highly ion-conducting interface between oxide-based solid electrolytes and electrodes is a challenge for establishing the manufacturing process of the cells.

Co-sintering at high temperatures is a widely used method to join oxide-based solid electrolytes and electrode materials as well as densification of the individual materials. Depending on the combination of an electrode material and a solid electrolyte, however, co-sintering often results in undesired side reactions which cause the decomposition of substances, instead of the formation of well-defined ion-conducting interfaces.[12−15] Even if they are bound to each other, highly resistive layers can be formed at their interfaces that severely impede the ion conduction.[16,17]

Received: April 6, 2025
Revised: July 1, 2025
Accepted: July 3, 2025
Published: July 9, 2025

https://doi.org/10.1021/acs.jpcc.5c02329
J. Phys. Chem. C 2025, 129, 12738−12749

Various approaches have been employed to construct the highly ion-conducting interfaces without the undesired side reactions, such as utilization of additives to lower the sintering temperature[18,19] and surface coating with ion-conducting and sinterable materials.[20,21] On the other hand, a comprehensive understanding of the reaction products after co-sintering the oxide-based solid electrolytes with the electrode materials is very important not only for fundamental inorganic chemistry but also to establish the rational manufacturing process for oxide-based ASSLIBs.

In addition to the combinations and compositions of electrode materials and solid electrolytes, the reaction products significantly depend on the sintering temperature[12,14] and atmosphere.[12,22] Among these tremendous parameters, it is very difficult to find the optimized sintering conditions to bind electrode materials and solid electrolytes without the occurrence of side reactions. Therefore, a highly reliable theory-based approach that can propose the optimized co-sintering conditions suitable for the given electrode materials and solid electrolytes is strongly desired.

Thermodynamic calculation is a powerful technique to predict the thermodynamically stable phases at given conditions such as chemical compositions (e.g., the number of elements),[23,24] atmospheres,[25,26] temperature[25,27,28] and electrochemical potential.[24,29] Zhu et al. performed first-principles density functional theory (DFT) calculations for various binary systems composed of an electrode material and a solid electrolyte at 0 K in vacuum.[29] In the case of $LiCoO_2$ (LCO) and LATP mixture, although $Li_{0.5}CoO_2$, Co_3O_4, Li_3PO_4, $LiAl_5O_8$, and TiO_2 were predicted as thermally stable phases, they concluded that LCO and LATP can remain unreacted because the decomposition energy (e.g., the difference of Gibbs energy before and after reaction) was relatively small. Miara et al. also performed first-principles DFT calculations of thermodynamically stable phases in vacuum to compare with actual reaction products formed by co-sintering LATP and spinel cathode materials such as $Li_2NiMn_3O_8$, $Li_2FeMn_3O_8$, and $LiCoMnO_4$ with a volume ratio of 1:1.[13] Their results showed that the experimentally identified reaction products at given temperatures were consistent with the thermodynamically stable phases predicted at much lower temperatures. They attributed this temperature inconsistency to the slow kinetics of ionic diffusion.

Understanding the origin that causes the discrepancy between experimental results and thermodynamic calculations is very important because it can lead to the development of a reliable tool which can predict the reaction products at given sintering conditions and even instantaneously propose the optimized sintering conditions to construct the well-defined solid electrolyte/electrode interfaces from given materials. As both LCO and LATP are stable in air, co-sintering them in air provides an ideal model for studying the reactivity of electrode active materials and solid electrolytes under realistic processing conditions. Previously, we have quantitatively identified the temperature-dependent reaction products of LCO and LATP composites with a volume ratio of 3:7 sintered under various conditions (temperature, time, particle size, and cooling rate) by a complementary approach integrated with X-ray diffraction (XRD) and X-ray absorption near edge structure (XANES).[14] The reaction was reasonably progressed by co-sintering the submicron-scale LCO and LATP for 8 h, while the reaction was significantly slowing down for 10−15 μm LATP coarse particles under the same sintering conditions. In addition, it has been reported that ASSLIBs containing LCO and LATP can be fabricated using an aerosol deposition process followed by low-temperature annealing, which minimizes undesired side reactions.[30] These findings emphasize the importance of understanding how LCO and LATP react under different processing conditions. In order to evaluate the reliability and applicability of thermodynamic calculations based on experimental results, a wide range of composite ratios exhibiting different reaction behaviors must be investigated. In the present study, we further analyzed the reaction products of cosintered LCO and LATP composites with volume ratios of 3:7, 5:5, and 7:3 by XRD and XANES and compared with the thermodynamically stable phases calculated using the FactSage thermochemical software and ab initio materials database taking into account oxygen partial pressure to discuss the origin of the discrepancy between the experiment and thermodynamic calculations.

METHODS

Sample Preparation. LCO with an average particle size of 0.5 μm and LATP with an average particle size of 0.7 μm were purchased from TOSHIMA Manufacturing. Pure LCO and LATP powders, as well as the mixtures of LCO and LATP powders with volume ratios of 3:7 (LCLA37), 5:5 (LCLA55), and 7:3 (LCLA73), were gently mixed for 1 h in a Zr mortar and then pressed at 2 t/cm^2 in a uniaxial die with a 10 mm diameter to produce a pellet. The weight ratios and molar ratios of LCLA37, LCLA55, and LCLA73 are 0.74:1, 1.73:1, and 4.03:1 and 2.90:1, 6.88:1, and 17.2:1, respectively. The examined volume ratios were selected to cover the composition range in which macroscopic percolation networks for both the electrode material and the solid electrolyte are expected based on Bruggeman's effective media theory.[31] The pellets were sintered at various temperatures ranging from 300 to 900 °C every 50 °C for 8 h in air. The rate of temperature increase and decrease was set to 5 °C/min.

XRD Measurements. The crystalline phases of sintered samples were identified by XRD measurements (SmartLab Rigaku, Japan) equipped with a monochromatized Cu Kα source ($\lambda_{\alpha 1}$ = 1.5405 Å) and a scintillation counter. All of the data were collected using the step-scan method with a step width of 0.005° and an acquisition time of 2 s per step, in the range of 10° to 90°. PDXL2 software (Rigaku, Japan) was used to conduct the Rietveld analysis (Figures S1−S3). Table S1 in the Supporting Information lists the input powder diffraction files for Rietveld analysis from the international center for diffraction data (ICDD).

X-ray Absorption Spectroscopy and XAFS Data Analysis. For XAFS measurements, the sintered pellets were powdered, diluted with boron nitride purchased from FUJIFILM Wako Pure Chemical, and reformed into pellets. Co K-edge and Ti K-edge XAFS measurements were conducted in transmission mode at BL9A and BL9C equipped with a silicon (111) double crystal monochromator, Photon Factory, High Energy Accelerator Research Organization in Tsukuba, Japan (KEK). The rejection of higher harmonics was achieved by 30% detuning the double crystal monochromator for Co K-edge measurements and applying a cylindrically bent Rh-coated mirror for Ti K-edge measurements. The storage ring was operated at 2.5 GeV and 450.0 mA. The X-ray photon energy was calibrated by using Co and Ti metal foils as a standard sample. The ATHENA program[32] was used to conduct XAFS data processing, such as energy scale

https://doi.org/10.1021/acs.jpcc.5c02329
J. Phys. Chem. C 2025, 129, 12738−12749

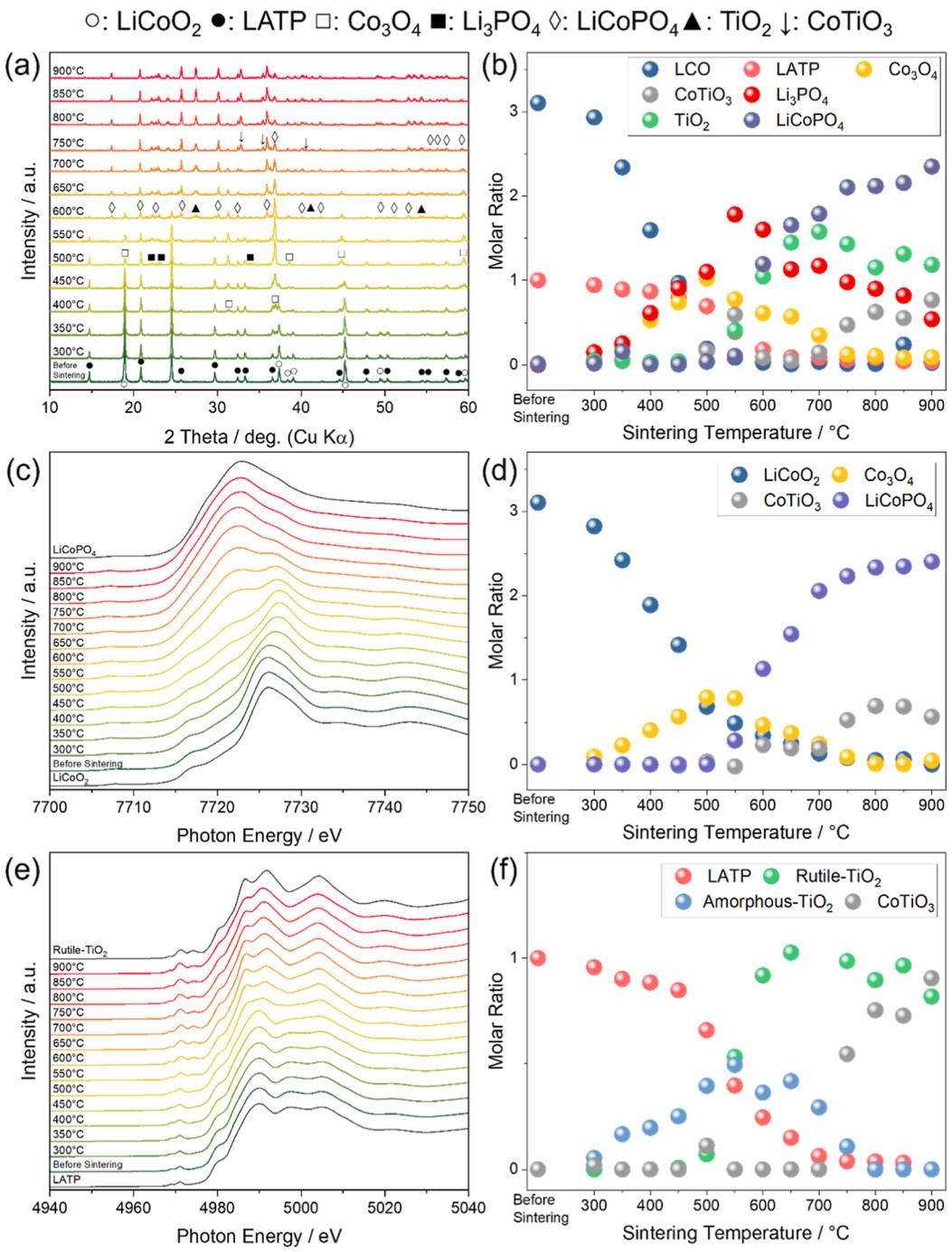

Figure 1. (a) XRD patterns of LCLA37 sintered at various temperatures, and (b) molar ratio of crystalline phases determined by Rietveld analysis of XRD patterns. (c) Normalized Co K-edge XANES spectra of LCLA37 sintered at various temperatures, and (d) molar ratio of Co-containing species determined by LCF of the XANES spectra. (e) Normalized Ti K-edge XANES spectra of LCLA37 sintered at various temperatures, and (f) molar ratio of Ti-containing species determined by LCF of the XANES spectra. (Reproduced from ref 14 with permission from the Royal Society of Chemistry).

calibrations, background subtraction, postedge normalization, and XANES analysis.

For linear combination analysis[33,34] of a series of XANES spectra arising from a mixture of LCO, LATP, and unknown products, principal component analysis (PCA) was performed. The concept of PCA is available from the literature.[35−39] In brief, PCA helps us to determine the number of components as eigenvectors that reproduce an experimental data set without an a priori assumption. In this study, we chose the number of components as the same number of eigenvectors that allow the PCA results to reproduce the experimental data set (Co or Ti K-edge XANES spectra) with a remnant of 0.005% or the number of Co- or Ti-containing crystalline phases detected by XRD. The reference compounds/spectra used for linear combination analysis (LCF) were selected by target transformation. In target transformation, linear combination fitting using a certain number of eigenvectors given by PCA is applied to each XANES spectrum of a potential reference compound, and the reference spectra used for LCF are determined in the order of the smallest mean square error of the residuals

https://doi.org/10.1021/acs.jpcc.5c02329
J. Phys. Chem. C 2025, 129, 12738−12749

between the XANES spectrum of the reference compound and linear combination of eigenvectors. The results of PCA and target transformation are listed in Tables S2−S13 in the Supporting Information.

LCF results of Co and Ti K-edge of LCO and LATP composites sintered at various temperatures are shown in Figures S4−S9 in the Supporting Information. Here, we note that the Co_2TiO_4 spinel phase observed by XRD patterns of LCLA55 sintered at various temperatures (see Result Section) is not included in the database.[40] Hence, it was synthesized with the procedure described in the literature[41] and used as a reference compound for Co K-edge and Ti K-edge XANES (see Supporting Information Section S3, Figure S10a,b). In addition, because both Co_2TiO_4 and $Li_4Ti_5O_{12}$ used for linear combination fitting of Ti K-edge XANES (Tables S5, S9 and S13) are spinel structures ($Fd\bar{3}m$), as shown in Figure S11, and their Ti cations are tetravalent (Ti^{4+}), the shapes of Ti K-edge XANES spectra of Co_2TiO_4 and $Li_4Ti_5O_{12}$ shown in Figure S10b are similar to each other. Thus, in this study, Co_2TiO_4 was selected as the representative of the spinel phase for the LCF of Co K-edge XANES (Tables S7 and S11) and $Li_4Ti_5O_{12}$ was excluded from the candidate.

The molar ratios of the reaction products were estimated, as in our previous work,[14] by combining the results of the Rietveld analysis of the XRD patterns and the LCF of the XANES spectra. First, the initial molar amounts of LCO and LATP were determined by Rietveld refinement, which defined the total Co and Ti contents in the sample. Next, the relative amounts of the Co- and Ti-containing phases were quantified by using the LCF of the XANES spectra to account for the fraction of amorphous species. The Co- and Ti-free phases were obtained directly from Rietveld analysis of the XRD patterns.

Thermogravimetry Measurements. Thermogravimetric analysis (TG) of LCLA37, LCLA55, and LCLA73 was performed using a STA2500 Regulus (NETZSCH, Germany) with a 90 mL/min air flow. The temperature program was set with a heating rate of 5 °C/min from room temperature to 900 °C. After a 1 h hold at 900 °C, it was cooled down to room temperature with a cooling rate of 5 °C/min. All of the measurements were carried out with samples of about 10 mg in Pt sample containers.

Thermodynamic Calculation. FactSage 8.2 (GTT-Technologies, Germany) and its database ab initio material project[42] (aiMP) 4.0 were used to estimate the reaction products in the LCO and LATP mixture with various volume ratios at different temperatures under atmospheric pressure (oxygen partial pressure, P_{O_2} = 0.21 atm).

RESULTS

Experimental Characterization of Reaction Products of LCLA37. We have previously determined the reaction products of LCLA37 in both crystalline and amorphous phases by complementary use of XRD and XANES.[14] Figure 1a,b shows the XRD patterns and Rietveld analysis of LCLA37 sintered at various temperatures. The molar ratio of LCO to LATP before sintering is 3.10:1, which is in good agreement with the initial molar ratio of 2.90:1. Although solely sintered pure LCO and LATP are stable up to 900 °C (Figures S12 and S13), LCO and LATP in LCLA37 start to react with each other at 300 °C to form Co_3O_4 and Li_3PO_4, and the crystalline phase of LCO disappears at 500 °C. From 300 to 500 °C, Li_3PO_4 forms probably due to the decomposition of LATP, but any Al- and/or Ti-containing species are absent, suggesting that these Al- and Ti-containing species are amorphous. LATP and the reaction products formed in the temperature range from 300 to 500 °C such as Co_3O_4, and Li_3PO_4 are consumed from 500 to 750 °C to form $LiCoPO_4$, rutile-TiO_2, and $CoTiO_3$. After sintering at 900 °C, Co^{3+} in the starting material LCO is completely reduced to Co^{2+} in $LiCoPO_4$ and $CoTiO_3$, while Ti^{4+} in the starting material LATP is unchanged in rutile-TiO_2 and $CoTiO_3$.

Figure 1c,e shows Co and Ti K-edge XANES spectra of LCLA37 sintered at various temperatures. The shape of the Co and Ti K-edge XANES spectrum of LCLA37 before sintering is identical to that of LCO with a relatively strong white line at around 7729 eV[14,43] and LATP with a preedge at around 4970 eV and a relatively weak white line at around 4989 eV.[14,44] With increasing sintering temperature, the absorption of the Co K-edge is shifted to the lower energy side, suggesting the reduction of Co^{3+} in LCO to Co^{2+}. This change becomes more remarkable at sintering temperatures above 500 °C, where most of the Co-containing species are reduced to Co^{2+} species such as $LiCoPO_4$ and $CoTiO_3$ as observed by XRD. On the other hand, the absorption of Ti K-edge remains unchanged after co-sintering throughout the temperature range, confirming that the Ti^{4+} in LATP remains as Ti^{4+} in rutile-TiO_2 and $CoTiO_3$ as observed by XRD.

Figure 1d,f shows the LCF results of Co and Ti K-edge XANES spectra of LCLA37 sintered at various temperatures using the XANES spectra of the reference compounds determined by PCA and target transformation. Consistent with the Rietveld analysis of XRD, the LCF analysis of XANES also shows that LCO (Figure 1d) and LATP (Figure 1f) start to decrease at 300 °C due to the reaction. At sintering temperatures between 300 and 500 °C, LCO and Co_3O_4 decreases and increases, respectively, and amorphous-TiO_2 forms due to the decomposition of LATP. At sintering temperatures between 500 and 700 °C, Co_3O_4, amorphous-TiO_2, and LATP decrease, and $LiCoPO_4$ and rutile-TiO_2 increase. At sintering temperatures between 700 and 900 °C, LCF of Co and Ti K-edge XANES shows the further decrease of Co_3O_4 and rutile-TiO_2, concurrently with the formation of $CoTiO_3$. Thus, the Co- and Ti-containing final products are $LiCoPO_4$, $CoTiO_3$, and rutile-TiO_2. There are two discrepancies between Rietveld analysis of XRD and LCF of XANES due to the insensitive nature of XRD to amorphous contents. Unlike the Rietveld analysis that shows the complete loss of LCO at 500 °C (Figure 1b), LCF of Co K-edge XANES indicates the presence of LCO up to 700 °C, suggesting the existence of amorphous and/or microcrystalline LCO. Moreover, amorphous-TiO_2 was observed in LCF of Ti K-edge XANES.

Figure 2 shows the TG curves of LCO, LATP, and LCLA37. From the TG curves, the weight loss values of LCO, LATP, and LCLA37 were 0.80%, 2.51%, and 5.21%, respectively. According to the fact that pure LCO and LATP are stable in the temperature range of 300−900 °C (Figures S12 and S13),[45,46] the weight loss of pure LCO and LATP should be due to the desorption of adsorbed water and volatile organic species possibly used as the precursor. Based on the weight loss of pure LCO (0.80%) and LATP (2.51%) and the weight ratio of LCO and LATP in LCLA37 (LCO/LATP = 0.74:1), the expected weight loss due to the desorption of adsorbed species from LCO and LATP in LCLA37 is estimated to be 0.34% and

https://doi.org/10.1021/acs.jpcc.5c02329
J. Phys. Chem. C 2025, 129, 12738−12749

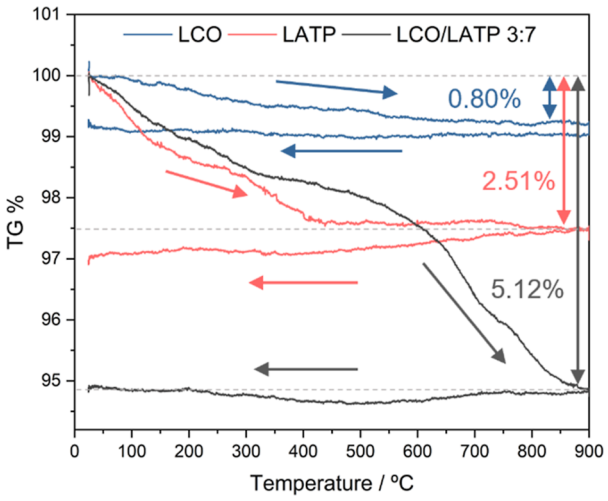

Figure 2. TG curves of pure LCO, LATP, and LCLA37.

1.44%, respectively. Thus, 3.43% out of 5.21% is attributable to the weight loss due to the chemical reactions such as the oxygen release accompanying the reduction of Co^{3+} to Co^{2+}. Because all the Co^{3+} in the starting material LCO is completely reduced to Co^{2+} species (XRD and Co K-edge XANES in Figure 1b,d), the weight loss due to the accompanying oxygen release is estimated to be 3.48% which is in good agreement with the experimental value, 3.43% obtained by TG. During the cooling process from 900 °C to room temperature in Figure 2, there is no weight change in the TG curve, indicating that no further reaction occurs.

Experimental Characterization of Reaction Products of LCLA55. Figure 3a,b shows the XRD patterns and Rietveld analysis of LCLA55 sintered at various temperatures. In the results of the Rietveld analysis (Figure 3b), the molar ratio of LCO to LATP before sintering, 7.08:1, is in good agreement with the initial molar ratio of 6.88:1. When LCLA55 is sintered at temperatures higher than 300 °C, LCO and LATP react with each other to form Co_3O_4 and Li_3PO_4. The amounts of Co_3O_4 and Li_3PO_4 increase with temperature up to 600 and 700 °C, respectively. Co_3O_4 starts to decrease from 600 °C simultaneously with the formation of a spinel phase with a lattice constant a = 8.4117(3) Å, which is different from that of Co_3O_4: a = 8.072 Å.[47] Based on the lattice parameter, this spinel phase is assignable to Co_2TiO_4 (a = 8.4440 Å)[48] or $Li_4Ti_5O_{12}$ (a = 8.3804 Å).[49] Considering the total amounts of Co and Ti in the samples (Figure S14), Co_2TiO_4 is the more reasonable substance. In the temperature range between 550 and 900 °C, first rutile-TiO_2 (550−700 °C) then $CoTiO_3$ (700−800 °C) and eventually Co_2TiO_4 form together with the decrease of Co_3O_4, suggesting the successive reaction of Co_3O_4 with TiO_2, $CoTiO_3$ and Co_2TiO_4. In addition, the peak position of the Co_3O_4 spinel phase shifted to the lower angle and that of the Co_2TiO_4 spinel phase shifted to the higher angle with increasing sintering temperature from 750 to 900 °C (Figure S15a), implying the formation of solid solutions of Li in Co_3O_4[50,51] and Li and Ti in Co_2TiO_4.[52−54]

Figure 3c,e shows Co and Ti K-edge XANES spectra of LCLA55 sintered at various temperatures. With increasing sintering temperature, the absorption of Co K-edge is shifted to the lower energy side, suggesting the reduction of Co^{3+} in LCO to Co^{2+}. This change corresponds to the formation of Co_3O_4, $CoTiO_3$, and Co_2TiO_4 with Co^{2+} as observed by XRD. On the other hand, the absorption of Ti K-edge does not shift, suggesting that the Ti^{4+} in LATP remains as Ti^{4+} in rutile-TiO_2, $CoTiO_3$, and Co_2TiO_4 as observed by XRD. Figure 3d,f shows the LCF results of Co and Ti K-edge XANES spectra of LCLA55 sintered at various temperatures using the XANES spectra of the reference compounds. The LCF results of Co K-edge and Ti K-edge XANES spectra are consistent with the Rietveld analysis; LCO and LATP decrease at 300 °C to form Co_3O_4, Co_3O_4 increases from 300 to 600 °C, and rutile-TiO_2 (550−700 °C), $CoTiO_3$ (700−900 °C), and eventually Co_2TiO_4 appear in turn together with the continuous decrease of Co_3O_4 from 600 to 900 °C. In addition to those crystalline phases, amorphous-TiO_2 is present from 300 to 700 °C, implying that amorphous-TiO_2 (300−700 °C) forms prior to rutile-TiO_2 (550−700 °C) as a result of the decomposition of LATP. Another difference between the XANES and XRD is the temperature range where $CoTiO_3$ exists. Both Co and Ti K-edge XANES detect $CoTiO_3$ from 700 to 900 °C, whereas it disappears at 800 °C in XRD, suggesting the existence of amorphous-$CoTiO_3$ from 800 to 900 °C.

Figure 4 shows the TG curve of LCLA55. The TG curve shows a weight loss of 4.41% after heating at 900 °C. Based on the weight loss of pure LCO (0.80%) and LATP (2.51%) and the weight ratio of LCO and LATP in LCLA55 (LCO/LATP = 1.73:1), the expected weight loss due to the desorption of adsorbed species from LCO and LATP in LCLA55 is estimated to be 0.51% and 0.89%, respectively. Thus, 3.01% of 4.41% can be attributed to the weight loss due to the chemical reactions. When approximately 57% of Co^{3+} in LCO of pristine LCLA55 is reduced to Co^{2+}, the weight loss due to the accompanying oxygen release coincides with 3%. Consequently, 43% of Co ions remain as Co^{3+} in the Co_3O_4 phase at 900 °C. However, the LCF of Co K-edge XANES shows that the amount of Co^{3+} is 37.1%, which is somewhat smaller than that estimated from the TG curves. This difference can be attributed to the formation of the solid solutions as mentioned above. In the present study (Figure 3a), the expansion of lattice constant of Co_3O_4 is evident by the peak shifts to the low-angle side in XRD, suggesting the formation of the solid solution of Li in Co_3O_4.[50,51] In this case, Co ions in Co_3O_4 can be partially oxidized for electroneutrality. Enlarged graphs (Figure S15a) clearly show the shift of the 311 diffraction peak of Co_3O_4 in LCLA55 sintered at 800 °C. The only Li-containing species at 900 °C is Li_3PO_4 and its molar amount of Li, 8.09 mol, is 0.29 mol less than the initial amount of Li in the pristine LCLA55 (molar amount of Li = 8.38 mol). When 0.29 mol of Li forms the solid solution with Co_3O_4, the amount of Co^{3+} is estimated to be 40.2% which is still larger than that determined by LCF of Co K-edge XANES. The remaining difference can be caused by the difference in sintering time between TG measurements (ramping at 5 °C/min with 1 h holding) and others (holding at each temperature for 8 h after ramping at 5 °C/min).

Experimental Characterization of Reaction Products of LCLA73. Figure 5a,b shows the XRD patterns and Rietveld analysis of LCLA73 sintered at various temperatures. In the results of the Rietveld analysis, the molar ratio of LCO to LATP before sintering, 20.6:1, is in reasonable agreement with the initial molar ratio of 17.2:1. At 300 °C, LCO and LATP start to react with each other to form Co_3O_4 and Li_3PO_4. The amount of LCO decreases, and those of Co_3O_4 and Li_3PO_4 increase with temperature up to 650 °C where LATP completely disappears. In LCLA73, an excess amount of

https://doi.org/10.1021/acs.jpcc.5c02329
J. Phys. Chem. C 2025, 129, 12738−12749

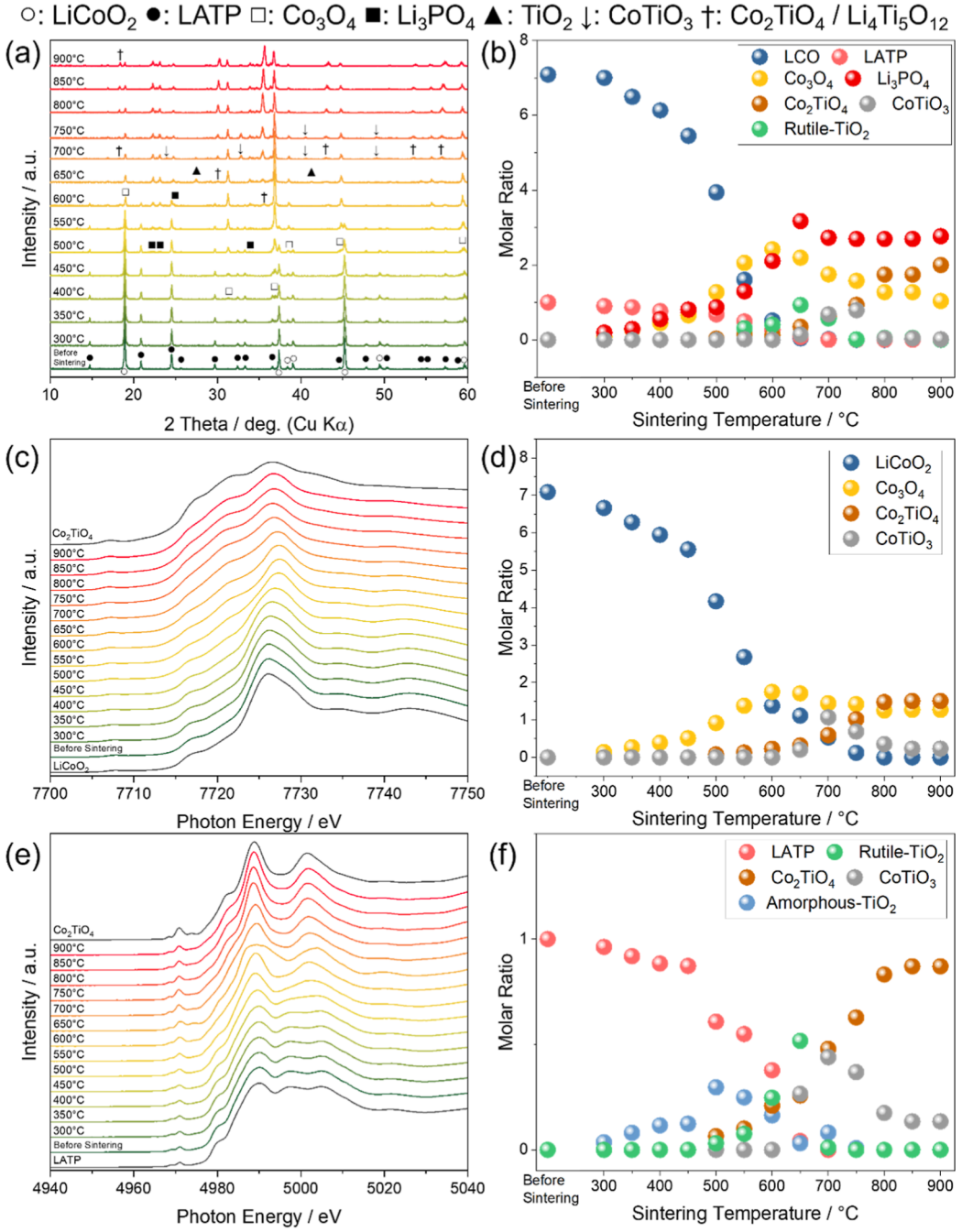

Figure 3. (a) XRD patterns of LCLA55 sintered at various temperatures, and (b) molar ratio of crystalline phases determined by Rietveld analysis of XRD patterns. (c) Normalized Co K-edge XANES spectra of LCLA55 sintered at various temperatures, and (d) molar ratio of Co-containing species determined by LCF of the XANES spectra. (e) Normalized Ti K-edge XANES spectra of LCLA55 sintered at various temperatures, and (f) molar ratio of Ti-containing species determined by LCF of the XANES spectra.

LCO is mixed with LATP, and therefore, a large portion of the LCO remains in the temperature range from 650 to 900 °C. Li_2TiO_3 forms at 650 °C and remains up to 900 °C. The full width at half-maximum of the diffraction peak from (311) planes of Co_3O_4 increases (Figure S15b), suggesting that Li forms the solid solution with some Co_3O_4.[50,51]

Figure 5c,e shows Co and Ti K-edge XANES spectra of LCLA73 sintered at various temperatures. Similarly, with those of LCLA37 and LCLA55, the absorption of the Co K-edge shifts to the lower energy side due to the formation of Co_3O_4 containing Co^{2+}, while the Ti K-edge remains unchanged. Figure 5d,f shows the LCF results of Co and Ti K-edge XANES spectra of LCLA73 sintered at various temperatures. The trendlines of LCO, LATP, and other substances are almost identical to those obtained by Rietveld analysis of XRD with a few exceptions. Co_2TiO_4 is absent in XRD throughout the temperature range (Figure 5b) but present in Co and Ti K-edge XANES between 550 and 900 °C (Figure 5d,f), suggesting the formation of amorphous- and/or microcrystalline Co_2TiO_4.

Figure 6 shows the TG curve of the LCLA73. The TG curve shows a gradual weight loss of 2.69% up to 800 °C, followed by a steep weight loss of 2.65% from 800 to 900 °C. Interestingly, a weight gain of 2.96% is observed in the cooling process. The

https://doi.org/10.1021/acs.jpcc.5c02329
J. Phys. Chem. C 2025, 129, 12738−12749

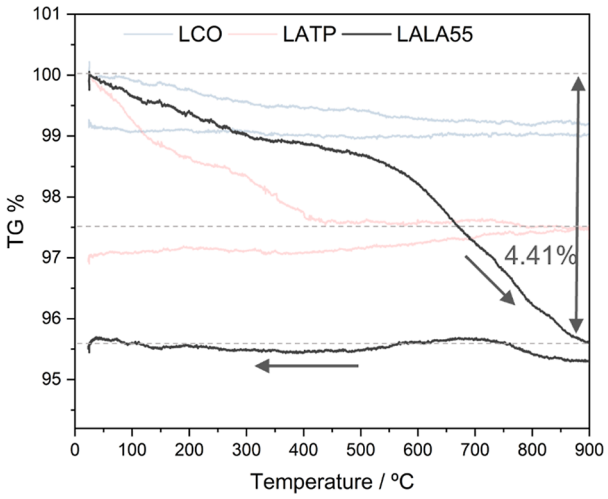

Figure 4. TG curves of pure LCO, LATP, and LCLA55.

former gradual weight losses similar to those observed for LCLA37 and LCLA55 should be due to the desorption of adsorbed species. The latter steep weight loss and gain in the cooling process are assignable to the reversible phase transition between Co_3O_4 and CoO that forms at 850 °C.[55,56] Considering the percentage of Co_3O_4 at 800 °C, determined by Rietveld analysis (Figure 5b), the amount of oxygen desorbed during this phase transition is estimated to be 2.61%, which is in reasonable agreement with the TG curve.

DISCUSSION

Figure 7 shows the comprehensive molar ratios of chemical species including both crystalline and amorphous phases obtained by XANES and XRD, in LCLA37, LCLA55, and LCLA73, after sintering at various temperatures. Al-containing species are absent in XRD. Additionally, it is challenging to precisely quantify the quantity of Al-containing species using Al K-edge XANES measurements in a standard transmission setup. This is because the attenuation length of X-rays in the corresponding energy region is relatively short, requiring extremely thin samples to ensure sufficient transmitted X-ray intensity. Hence, all of the Al-containing species contained in the composite are assumed to be Al_2O_3.

Thermodynamics Calculation by FactSage 8.2. Figure 8a–c shows the thermodynamically stable phases in LCLA37, LCLA55, and LCLA73 at various temperatures with an oxygen partial pressure of P_{O_2} = 0.21, and Table S14 compares them with the experimentally identified ones.

At 900 °C for LCLA37, the combination of calculated thermodynamically stable phases $LiCoPO_4$, TiO_2, Li_3PO_4, and $CoTi_2O_5$ (Figure 8a) was in reasonable agreement with that of major reaction products, $LiCoPO_4$, TiO_2, Li_3PO_4, and $CoTiO_3$ (Figure 7a), with a discrepancy that $CoTi_2O_5$ was predicted instead of the experimentally detected $CoTiO_3$. In contrast to the fact that the thermodynamic calculations predicted stable phases at given temperatures, the reaction products were analyzed at room temperature after the samples were cooled from the sintering temperatures. Thus, one may attribute the discrepancy to the phase transformation during the cooling process because $CoTi_2O_5$ is a high temperature phase which forms in the temperature range higher than 1140 °C.[57,58] However, no sign of a phase transformation was observed in the TG curve during the cooling process (Figure 2). In addition, it was reported that $CoTi_2O_5$ forms at 1140 °C[57,58] which is much higher than the sintering temperatures used in the present study.

Another possibility is the formation of secondary stable phases instead of primary ones. The sum of the Gibbs free energies of $CoTiO_3$ and TiO_2 at room temperature is comparable to that of $CoTi_2O_5$, as shown in eq 1.

$$CoTiO_3\ (-1262.6\ kJ) + TiO_2\ (-992.1\ kJ) \Leftrightarrow CoTi_2O_5\ (-2263.0\ kJ) \quad (1)$$

When $CoTi_2O_5$ was replaced with $CoTiO_3$ in Figure 8d, the combination and molar ratio of thermodynamically predicted stable phases and experimentally detected reaction products matched each other perfectly.

The compositions of predicted thermodynamically stable phases were almost constant in the temperature range between 500 and 900 °C. In contrast, the molar ratios of experimentally identified species significantly changed as the temperature became lower from 900 to 500 °C; $CoTiO_3$, $LiCoPO_4$, and TiO_2 decreased and Li_3PO_4, Co_3O_4, LATP, and LCO gradually increased. This suggests the existence of a relatively slow kinetic process. In fact, the reaction products at 500 °C, 600 °C, and 700 °C were significantly changed by elongating the sintering time from 8 h to 2 weeks (Figure S16), especially for 500 °C, so that the combination and molar ratios of reaction products were in better agreement with those of the thermodynamically stable phases; the molar ratio of Li_3PO_4, Co_3O_4, LATP, and LCO decreased and those of $LiCoPO_4$, TiO_2, and $CoTiO_3$ increased (Figure S16a). Furthermore, when the LATP powder with an average particle size of 0.1 μm (Figure S17a), which is smaller than that of the regular one (0.7 μm, Figure S17b), was cosintered with the LCO powder at 500 °C, 600 °C, and 700 °C for 8 h, the reaction products (Figure S18), Co_3O_4, $LiCoPO_4$, rutile-TiO_2, Li_3PO_4, and $CoTiO_3$ became more consistent with the thermodynamically stable phases (Figure S18). These results imply that the diffusion of metal cations might be kinetically slow at the low temperature.[59,60]

The reaction products and thermodynamically stable phases completely differ from each other in the temperature range lower than 500 °C. Eventually, the starting materials LCO and LATP became the majority species. In this temperature range from 300 to 450 °C, thermodynamic calculations suggested the formation of $Li_{0.5}CoO_2$. However, $Li_{0.5}CoO_2$, which is the Li-extracted LCO with the original layered structure, cannot be distinguished from LCO in XRD.

At 900 °C for LCLA55, $CoTiO_3$, Co_2TiO_4, Li_3PO_4, and Co_3O_4 were the major reaction products, whereas $Li_2CoTi_3O_8$, $LiCoPO_4$, Li_3PO_4, and CoO were predicted as the thermodynamically stable phases. $Li_2CoTi_3O_8$, $LiCoPO_4$, and CoO were predicted by thermodynamic calculations, instead of experimentally detected $CoTiO_3$, Co_2TiO_4, and Co_3O_4. This discrepancy can also be due to the existence of another possible combination of thermally stable phases. For example, the sum of the Gibbs free energies of Li_3PO_4 and $3Co_2TiO_4$ at room temperature is comparable to that of $LiCoPO_4$, $Li_2CoTi_3O_8$, and 4CoO, as shown in eq 2.

$$Li_3PO_4\ (-1262.6\ kJ) + 3Co_2TiO_4\ (-1496.2\ kJ \times 3) \Leftrightarrow LiCoPO_4\ (-1639.8\ kJ) + Li_2CoTi_3O_8\ (-3984.2\ kJ) + 4CoO\ (-266.8\ kJ \times 4) \quad (2)$$

https://doi.org/10.1021/acs.jpcc.5c02329
J. Phys. Chem. C 2025, 129, 12738−12749

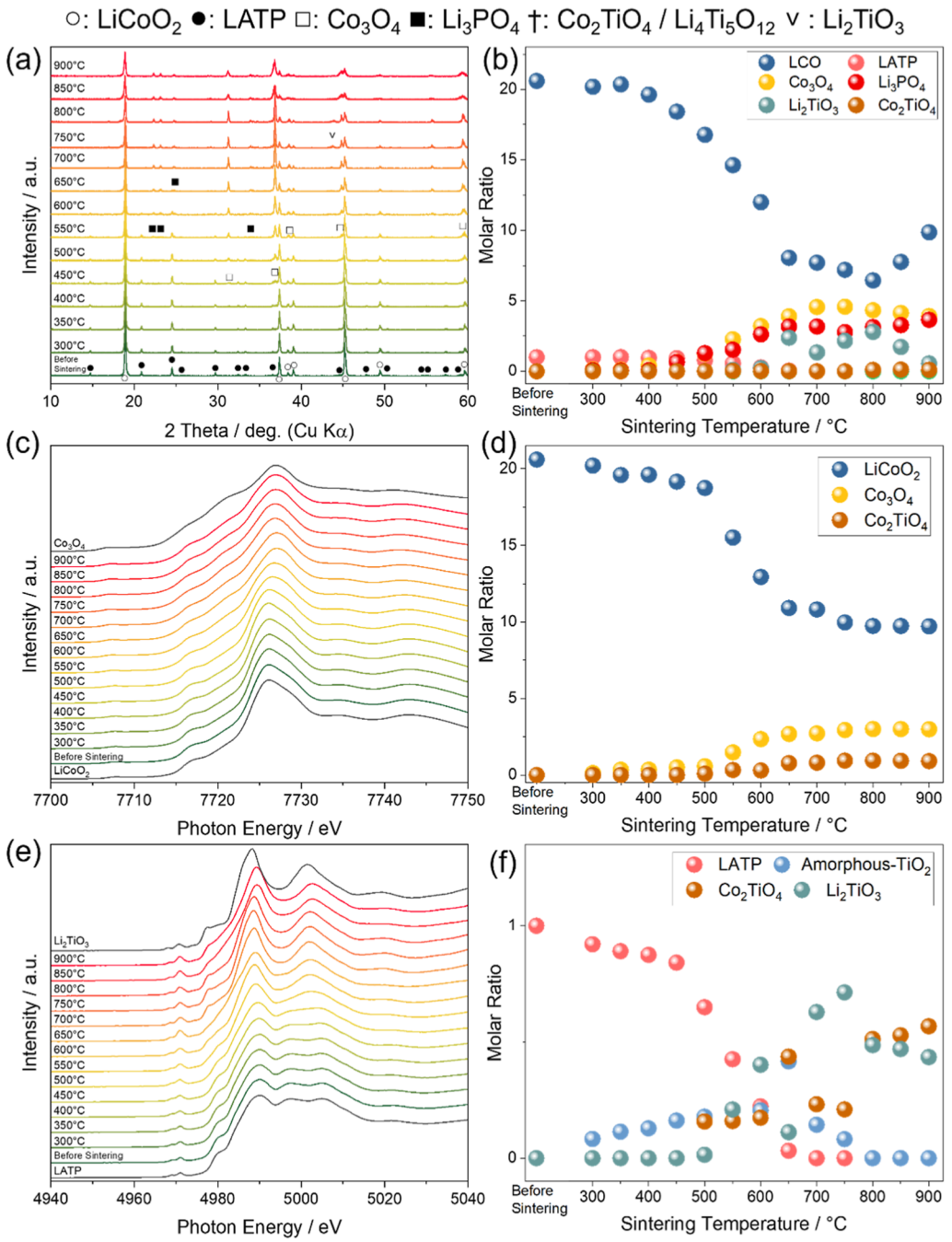

Figure 5. (a) XRD patterns of LCLA73 sintered at various temperatures, and (b) molar ratio of crystalline phases determined by Rietveld analysis of XRD patterns. (c) Normalized Co K-edge XANES spectra of LCLA73 sintered at various temperatures, and (d) molar ratio of Co-containing species determined by LCF of the XANES spectra. (e) Normalized Ti K-edge XANES spectra of LCLA73 sintered at various temperatures, and (f) molar ratio of Ti-containing species determined by LCF of the XANES spectra.

Even after $LiCoPO_4$, $Li_2CoTi_3O_8$, and 4CoO of the primary thermodynamically stable phases (Figure 8b) were replaced with the members of secondary ones such as Li_3PO_4 and $3Co_2TiO_4$, a small amount of CoO was still present in Figure S19a. CoO is also a typical high temperature phase which forms in the temperature range higher than 850 °C,[55,56] and thus, it can be transformed into Co_3O_4 during the cooling process from the sintering temperature. Indeed, a mass gain was observed at around 770 °C in the TG curve during the cooling process (Figure 4), confirming the transformation of CoO to Co_3O_4. Thus, in addition to the replacement according to eq 2, the remaining CoO was further converted to Co_3O_4, as shown in Figure S19b. It shows that the composition and molar ratios became more consistent with those of experimentally detected reaction products. One may be concerned with the fact that the observed mass gain in the TG curve (Figure 4) was somewhat smaller than that required to convert all the remaining CoO into Co_3O_4. This incompletion can be interpreted as the formation of a solid solution of Li and Co_3O_4 during sintering as evidenced by broadening of diffraction peaks (Figure S15a), which suppressed the phase transition between Co_3O_4 and CoO.

Except for the replacement of $Li_2CoTi_3O_8$ and $LiCoPO_4$ with $CoTiO_3$ and TiO_2 from 900 to 850 °C, the composition

https://doi.org/10.1021/acs.jpcc.5c02329
J. Phys. Chem. C 2025, 129, 12738−12749

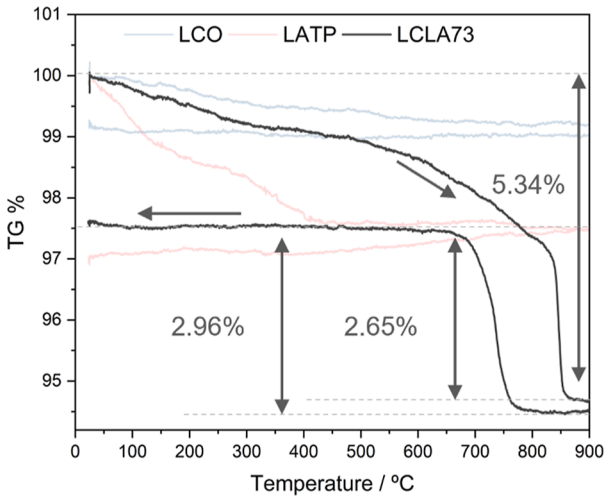

Figure 6. TG curves of pure LCO, LATP, and LCLA73.

of predicted thermally stable phases was substantially identical in the temperature range between 550 and 850 °C. In contrast, the composition of reaction products gradually changed as the temperature became lower from 900 °C, so that the molar ratios of Co_2TiO_4, Li_3PO_4, and Co_3O_4 decreased simultaneously with increasing those of starting materials such as LCO and LATP. The elongation of sintering time from 8 h to 2 weeks produced the reaction products similar to the predicted thermally stable phases at 600 and 700 °C (Figure S16e,f), suggesting the slow kinetics and insufficient sintering time for the lower temperature range. LCO and LATP became the dominant species.

After sintering LCLA73 at 900 °C, $LiCoO_2$, Co_3O_4, Li_3PO_4, Li_2TiO_3, and Co_2TiO_4 were identified by XANES and XRD (Figure 7a), although $LiCoO_2$, CoO, Li_3PO_4, and Li_2TiO_3 were predicted thermodynamically stable phases (Figure 8b). Because a mass gain assignable to the transformation of CoO to Co_3O_4 was clearly observed at around 750 °C in the TG curve during the cooling process (Figure 6), CoO was replaced with Co_3O_4, as shown in Figure 8f. The resulting composition and molar ratios of thermally stable phases and experimentally detected reaction products such as Li_3PO_4, Co_3O_4, and LCO became more consistent with each other in the temperature range between 650 and 900 °C.

Li_2TiO_3 and Co_2TiO_4 formed by sintering LCLA73 in the temperature range between 550 and 900 °C were the minor inconsistent species from the predicted thermally stable phases. Although Co_2TiO_4 was absent in the thermodynamic calculations, $Li_2CoTi_3O_8$ which is a solid solution of Li and Ti ions in the spinel structure substantially identical to Co_2TiO_4 (Figure S11) was predicted in the temperature range from 500 to 850 °C. Thus, these species can be interconverted to each other at given conditions with certain kinetics. Although thermodynamic calculations proposed the decomposition of LATP and LCO to Li_3PO_4 and $Li_{0.5}CoO_2$, respectively, almost all the starting materials remained unreacted in the low temperature range from 300 to 450 °C, probably due to the slow kinetics and insufficient sintering time.

The results presented here demonstrate that thermodynamic calculations can accurately predict reaction products formed at high temperatures. Therefore, these calculations are useful for screening material combinations and sintering conditions to prevent undesired side reactions. Conversely, the reaction progress was significantly suppressed at lower temperatures. This suggests that even material combinations that are expected to thermodynamically decompose may remain unreacted due to kinetic constraints such as slow ionic diffusion. Introducing a kinetic perspective into thermodynamic calculations may enable the construction of interfaces that function as batteries while preventing the formation of highly resistive reaction products that hinder ionic conduction.

CONCLUSIONS

The reaction products formed during co-sintering of LCO and LATP with three different compositions at various temperatures in air were quantitatively identified by XRD and XANES and compared with the thermodynamically stable phases calculated at various temperatures under the oxygen partial pressure of 0.21. Overall, the reaction products after sintering the composites of submicrometer-scale LCO and LATP powders at high temperatures, especially at 900 °C, tend to be well-reproduced by thermodynamic calculations. However, one may need to consider not only the primary combination composed of the most stable phases but also the alternative combinations composed of the secondary stable phases whose sum of Gibbs free energies is comparable to that of the primary combination to reproduce the experimentally identified phases. Another important factor that causes the gap between the experimentally identified and theoretically predicted phases is the cooling process. In contrast to the prediction of

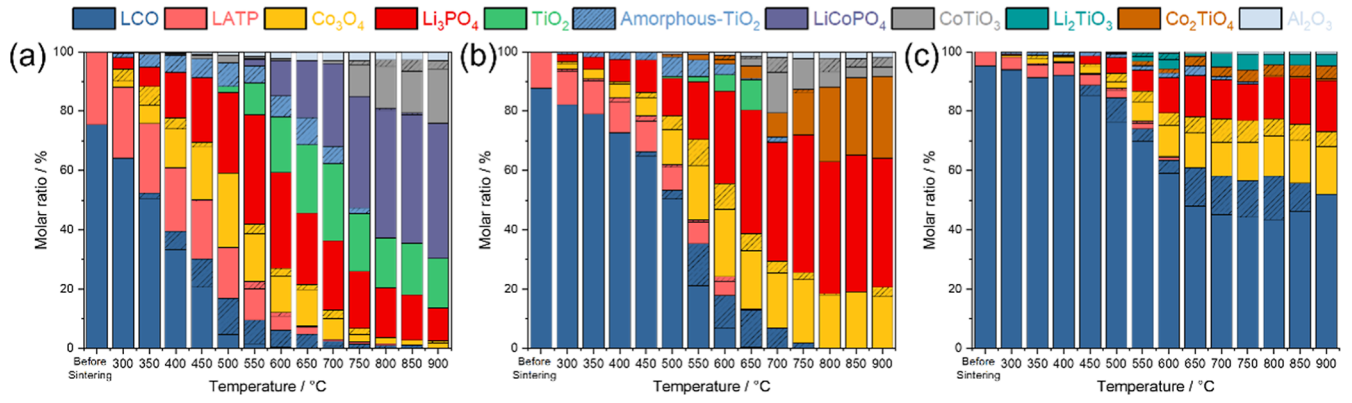

Figure 7. Molar ratio of chemical species in (a) LCLA37, (b) LCLA55, and (c) LCLA73 determined by Rietveld analysis of the XRD patterns and LCF of the XANES spectra. Shaded areas correspond to amorphous or microcrystalline phases.

https://doi.org/10.1021/acs.jpcc.5c02329
J. Phys. Chem. C 2025, 129, 12738−12749

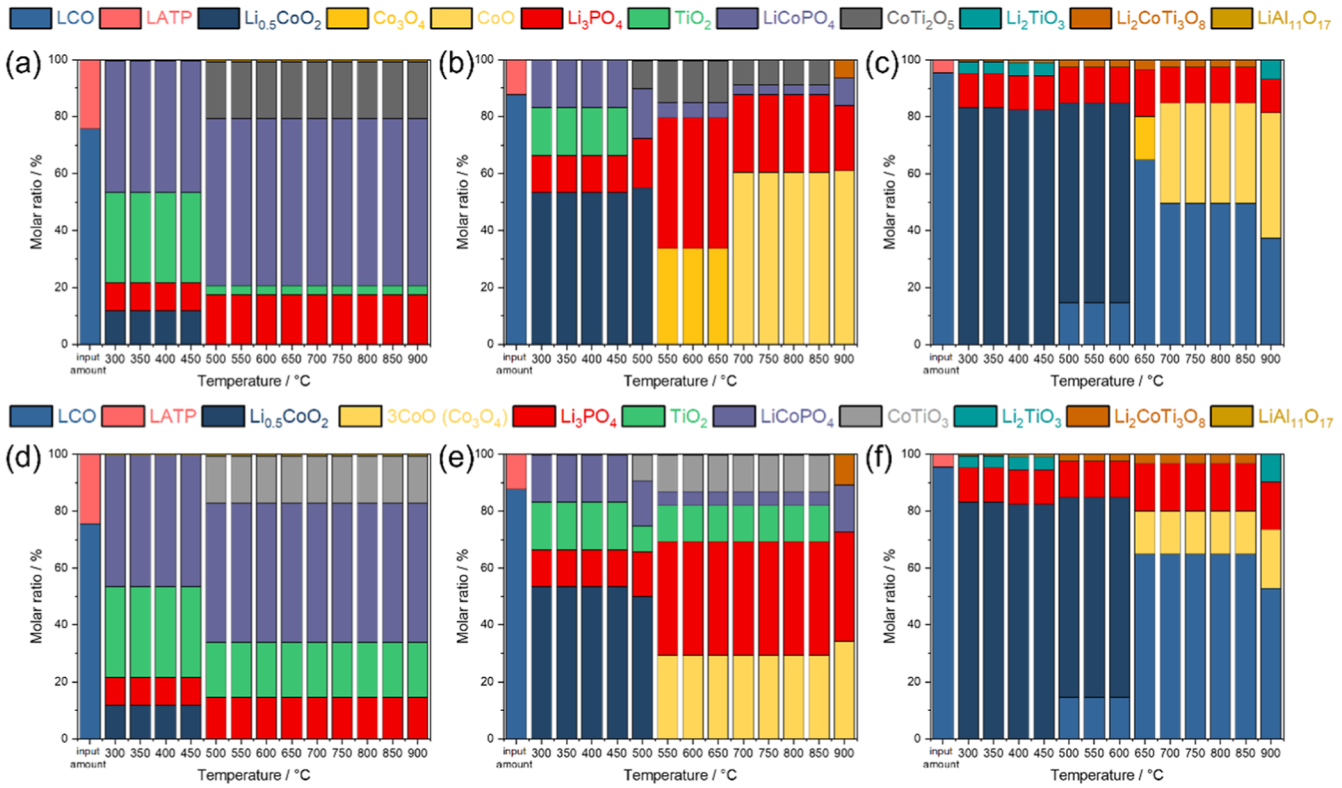

Figure 8. Molar amount of thermodynamically stable phase in (a) LCLA37, (b) LCLA55, and (c) LCLA73 calculated at various temperatures with an oxygen partial pressure of P_{O_2} = 0.21 and after conversion of the high temperature phase (CoO and $CoTi_2O_5$) to the low temperature phase (Co_3O_4, TiO_2 and $CoTiO_3$) in (d) LCLA37, (e) LCLA55, and (f) LCLA73.

thermodynamically stable phases at each temperature, the product analysis was performed at room temperature after cooling from the sintering temperatures, and thus, one needs to consider the phase transformations of high temperature species during this process to close the gap. As the sintering temperatures became lower from 900 °C, their discrepancy became more prominent due to the slow kinetic process and insufficient sintering time; starting materials and reaction products increased and decreased, respectively. During sintering, the experimentally observed phases often reflect kinetically favored states rather than thermodynamic equilibrium. While predicting nucleation behavior in reaction phases remains a challenge, more accurate insights into the formation and evolution of reaction products may be obtained by incorporating kinetic considerations through methods, such as the phase-field approach. Such improvements could eventually transform thermodynamic calculations into a practical tool for predicting possible side reactions, sinterable material combinations, and optimal sintering conditions, reducing the need for experimentation.

■ ASSOCIATED CONTENT

Supporting Information

The Supporting Information is available free of charge at https://pubs.acs.org/doi/10.1021/acs.jpcc.5c02329.

List of the input powder diffraction files for the Rietveld analysis from the ICDD, results of the Rietveld analysis of the XRD patterns, results of the PCA and target transformation, results of the LCF of the Co and Ti K-edge XANES spectra, detail of the description of ordered and disordered $Li_{4-2x}Co_{3x}Ti_{5-x}O_{12}$ spinel structures and Co_2TiO_4 spinel structure, thermal stability of pure LCO and LATP, additional data for spinel phase in LCLA55 and LCLA73, comparison between the thermodynamic calculation results and the experimental data, and experimental results with prolonged sintering time and LATP with different particle sizes (PDF)

■ AUTHOR INFORMATION

Corresponding Author

Takuya Masuda − *Research Center for Energy and Environmental Materials, National Institute for Materials Science (NIMS), Tsukuba, Ibaraki 305-0044, Japan; Graduate School of Chemical Sciences and Engineering, Hokkaido University, Sapporo, Hokkaido 060-0810, Japan;* orcid.org/0000-0001-7462-2177; Email: masuda.takuya@nims.go.jp

Authors

Fumihiko Ichihara − *Research Center for Energy and Environmental Materials, National Institute for Materials Science (NIMS), Tsukuba, Ibaraki 305-0044, Japan*

Shogo Miyoshi − *Research Center for Energy and Environmental Materials, National Institute for Materials Science (NIMS), Tsukuba, Ibaraki 305-0044, Japan;* orcid.org/0000-0003-0375-1187

Machiko Ode − *Research Center for Structural Materials, National Institute for Materials Science (NIMS), Tsukuba, Ibaraki 305-0047, Japan*

Complete contact information is available at: https://pubs.acs.org/10.1021/acs.jpcc.5c02329

https://doi.org/10.1021/acs.jpcc.5c02329
J. Phys. Chem. C 2025, 129, 12738−12749

Notes

The authors declare no competing financial interest.

■ ACKNOWLEDGMENTS

The authors would like to acknowledge the financial support provided by the Materials Processing Science project "Materealize" of the Ministry of Education, Culture, Sports, Science and Technology of Japan (MEXT; grant no. JPMXP0219207397). Synchrotron radiation experiments were performed as projects approved by the High Energy Accelerator Research Organization (KEK) (Proposal No. 2021G133 and No. 2023G131).

■ REFERENCES

(1) Castelvecchi, D.; Stoye, E. World-changing batteries win Nobel. *Nature* **2019**, *574*, 308.
(2) Orikasa, Y.; Yamamoto, K.; Shimizu, T.; Uchimoto, Y. Multiscale and hierarchical reaction mechanism in a lithium-ion battery. *Chem. Phys. Rev.* **2022**, *3* (1), 011305.
(3) Banerjee, A.; Wang, X.; Fang, C.; Wu, E. A.; Meng, Y. S. Interfaces and Interphases in All-Solid-State Batteries with Inorganic Solid Electrolytes. *Chem. Rev.* **2020**, *120* (14), 6878−6933.
(4) Chen, R.; Li, Q.; Yu, X.; Chen, L.; Li, H. Approaching Practically Accessible Solid-State Batteries: Stability Issues Related to Solid Electrolytes and Interfaces. *Chem. Rev.* **2020**, *120* (14), 6820−6877.
(5) Gao, Z.; Sun, H.; Fu, L.; Ye, F.; Zhang, Y.; Luo, W.; Huang, Y. Promises, Challenges, and Recent Progress of Inorganic Solid-State Electrolytes for All-Solid-State Lithium Batteries. *Adv. Mater.* **2018**, *30* (17), No. e1705702.
(6) Aono, H.; Sugimoto, E.; Sadaoka, Y.; Imanaka, N.; Adachi, G.-y. Electrical property and sinterability of $LiTi_2(PO_4)_3$ mixed with lithium salt (Li_3PO_4 or Li_3BO_3). *Solid State Ionics* **1991**, *47* (3), 257−264.
(7) Aono, H.; Imanaka, N.; Adachi, G.-y. High Li^+ Conducting Ceramics. *Acc. Chem. Res.* **1994**, *27* (9), 265−270.
(8) Bohnke, O.; Bohnke, C.; Fourquet, J. L. Mechanism of ionic conduction and electrochemical intercalation of lithium into the perovskite lanthanum lithium titanate. *Solid State Ionics* **1996**, *91* (1), 21−31.
(9) Yashima, M.; Itoh, M.; Inaguma, Y.; Morii, Y. Crystal Structure and Diffusion Path in the Fast Lithium-Ion Conductor $La_{0.62}Li_{0.16}TiO_3$. *J. Am. Chem. Soc.* **2005**, *127* (10), 3491−3495.
(10) Thangadurai, V.; Kaack, H.; Weppner, W. J. F. Novel Fast Lithium Ion Conduction in Garnet-Type $Li_5La_3M_2O_{12}$ (M = Nb, Ta). *J. Am. Ceram. Soc.* **2003**, *86* (3), 437−440.
(11) Murugan, R.; Thangadurai, V.; Weppner, W. Fast Lithium Ion Conduction in Garnet-Type $Li_7La_3Zr_2O_{12}$. *Angew. Chem., Int. Ed.* **2007**, *46* (41), 7778−7781.
(12) Gellert, M.; Dashjav, E.; Grüner, D.; Ma, Q.; Tietz, F. Compatibility study of oxide and olivine cathode materials with lithium aluminum titanium phosphate. *Ionics* **2018**, *24* (4), 1001−1006.
(13) Miara, L.; Windmuller, A.; Tsai, C. L.; Richards, W. D.; Ma, Q.; Uhlenbruck, S.; Guillon, O.; Ceder, G. About the Compatibility between High Voltage Spinel Cathode Materials and Solid Oxide Electrolytes as a Function of Temperature. *ACS Appl. Mater. Interfaces* **2016**, *8* (40), 26842−26850.
(14) Ichihara, F.; Miyoshi, S.; Masuda, T. Co-sintering process of $LiCoO_2$ cathodes and NASICON-type LATP solid electrolytes studied by X-ray diffraction and X-ray absorption near edge structure. *Phys. Chem. Chem. Phys.* **2022**, *24* (42), 25878−25884.
(15) Yu, C.-Y.; Choi, J.; Anandan, V.; Kim, J.-H. High-Temperature Chemical Stability of $Li_{1.4}Al_{0.4}Ti_{1.6}(PO_4)_3$ Solid Electrolyte with Various Cathode Materials for Solid-State Batteries. *J. Phys. Chem. C* **2020**, *124* (28), 14963−14971.
(16) Kato, T.; Hamanaka, T.; Yamamoto, K.; Hirayama, T.; Sagane, F.; Motoyama, M.; Iriyama, Y. In-situ $Li_7La_3Zr_2O_{12}/LiCoO_2$ interface modification for advanced all-solid-state battery. *J. Power Sources* **2014**, *260*, 292−298.
(17) Kato, T.; Yoshida, R.; Yamamoto, K.; Hirayama, T.; Motoyama, M.; West, W. C.; Iriyama, Y. Effects of sintering temperature on interfacial structure and interfacial resistance for all-solid-state rechargeable lithium batteries. *J. Power Sources* **2016**, *325*, 584−590.
(18) Han, F.; Yue, J.; Chen, C.; Zhao, N.; Fan, X.; Ma, Z.; Gao, T.; Wang, F.; Guo, X.; Wang, C. Interphase Engineering Enabled All-Ceramic Lithium Battery. *Joule* **2018**, *2* (3), 497−508.
(19) Hayashi, N.; Watanabe, K.; Shimanoe, K. Low-temperature sintering characteristics and electrical properties of Ca- and Bi-doped $Li_7La_3Zr_2O_{12}$ electrolyte containing Li_3BO_3 additive. *J. Mater. Chem. A* **2023**, *11* (4), 2042−2053.
(20) Li, S.-C.; Yu, J.-G. A well-designed $CoTiO_3$ coating for uncovering and manipulating interfacial compatibility between $LiCoO_2$ and $Li_{1.3}Al_{0.3}Ti_{1.7}(PO_4)_3$ in high temperature zone. *Appl. Surf. Sci.* **2020**, *526*, 146601.
(21) Ren, Y.; Wachsman, E. D. All Solid-State Li/LLZO/LCO Battery Enabled by Alumina Interfacial Coating. *J. Electrochem. Soc.* **2022**, *169* (4), 040529.
(22) Uhlenbruck, S.; Dornseiffer, J.; Lobe, S.; Dellen, C.; Tsai, C.-L.; Gotzen, B.; Sebold, D.; Finsterbusch, M.; Guillon, O. Cathode-electrolyte material interactions during manufacturing of inorganic solid-state lithium batteries. *J. Electroceram.* **2017**, *38* (2), 197−206.
(23) Richards, W. D.; Miara, L. J.; Wang, Y.; Kim, J. C.; Ceder, G. Interface Stability in Solid-State Batteries. *Chem. Mater.* **2016**, *28* (1), 266−273.
(24) Nolan, A. M.; Zhu, Y.; He, X.; Bai, Q.; Mo, Y. Computation-Accelerated Design of Materials and Interfaces for All-Solid-State Lithium-Ion Batteries. *Joule* **2018**, *2* (10), 2016−2046.
(25) Ong, S. P.; Wang, L.; Kang, B.; Ceder, G. Li−Fe−P−O_2 Phase Diagram from First Principles Calculations. *Chem. Mater.* **2008**, *20* (5), 1798−1807.
(26) Ong, S. P.; Jain, A.; Hautier, G.; Kang, B.; Ceder, G. Thermal stabilities of delithiated olivine MPO_4 (M = Fe, Mn) cathodes investigated using first principles calculations. *Electrochem. Commun.* **2010**, *12* (3), 427−430.
(27) Wang, L.; Maxisch, T.; Ceder, G. A First-Principles Approach to Studying the Thermal Stability of Oxide Cathode Materials. *Chem. Mater.* **2007**, *19* (3), 543−552.
(28) Urban, A.; Seo, D.-H.; Ceder, G. Computational understanding of Li-ion batteries. *npj Comput. Mater.* **2016**, *2* (1), 16002.
(29) Zhu, Y.; He, X.; Mo, Y. First principles study on electrochemical and chemical stability of solid electrolyte−electrode interfaces in all-solid-state Li-ion batteries. *J. Mater. Chem. A* **2016**, *4* (9), 3253−3266.
(30) Sakakura, M.; Suzuki, Y.; Yamamoto, T.; Yamamoto, Y.; Motoyama, M.; Iriyama, Y. Low-Resistive $LiCoO_2/Li_{1.3}Al_{0.3}Ti_2(PO_4)_3$ Interface Formation by Low-Temperature Annealing Using Aerosol Deposition. *Energy Technol.* **2021**, *9* (5), 2001059.
(31) McLachlan, D. S.; Blaszkiewicz, M.; Newnham, R. E. Electrical Resistivity of Composites. *J. Am. Ceram. Soc.* **1990**, *73* (8), 2187−2203.
(32) Newville, M. IFEFFIT: interactive XAFS analysis and FEFF fitting. *J. Synchrotron Radiat.* **2001**, *8* (2), 322−324.
(33) Lengke, M. F.; Ravel, B.; Fleet, M. E.; Wanger, G.; Gordon, R. A.; Southam, G. Mechanisms of Gold Bioaccumulation by Filamentous Cyanobacteria from Gold(III)−Chloride Complex. *Environ. Sci. Technol.* **2006**, *40* (20), 6304−6309.
(34) Abe, H.; Niwa, Y.; Kimura, M. A surface sensitive hard X-ray spectroscopic method applied to observe the surface layer reduction reaction of Co oxide to Co metal. *Phys. Chem. Chem. Phys.* **2020**, *22* (43), 24974−24977.
(35) Ressler, T.; Wong, J.; Roos, J.; Smith, I. L. Quantitative Speciation of Mn-Bearing Particulates Emitted from Autos Burning (Methylcyclopentadienyl)manganese Tricarbonyl-Added Gasolines Using XANES Spectroscopy. *Environ. Sci. Technol.* **2000**, *34* (6), 950−958.

https://doi.org/10.1021/acs.jpcc.5c02329
J. Phys. Chem. C 2025, 129, 12738−12749

(36) Beauchemin, S.; Hesterberg, D.; Beauchemin, M. Principal Component Analysis Approach for Modeling Sulfur K-XANES Spectra of Humic Acids. *Soil Sci. Soc. Am. J.* **2002**, *66* (1), 83−91.
(37) Beauchemin, S.; Hesterberg, D.; Chou, J.; Beauchemin, M.; Simard, R. R.; Sayers, D. E. Speciation of Phosphorus in Phosphorus-Enriched Agricultural Soils Using X-Ray Absorption Near-Edge Structure Spectroscopy and Chemical Fractionation. *J. Environ. Qual.* **2003**, *32* (5), 1809−1819.
(38) Fernandez-Garcia, M.; Marquez Alvarez, C.; Haller, G. L. XANES-TPR Study of Cu-Pd Bimetallic Catalysts: Application of Factor Analysis. *J. Phys. Chem.* **1995**, *99* (33), 12565−12569.
(39) Gaur, A.; Shrivastava, B. D. Speciation using X-ray absorption fine structure (XAFS). *Rev. J. Chem.* **2015**, *5* (4), 361−398.
(40) Ishii, M.; Nagao, H.; Tanabe, K.; Matsuda, A.; Yoshikawa, H. *"MDR XAFS DB". Materials Data Repository*; National Institute for Materials Science, 2021.
(41) Ghosh, S.; Singh, S.; Joshi, D. C.; Pramanik, P.; Ghosh, S.; Mishra, P. K.; Thota, S. Role of dilution on the electronic structure and magnetic ordering of spinel cobaltites. *Phys. Rev. B* **2018**, *98* (23), 235119.
(42) Ong, S. P.; Richards, W. D.; Jain, A.; Hautier, G.; Kocher, M.; Cholia, S.; Gunter, D.; Chevrier, V. L.; Persson, K. A.; Ceder, G. Python Materials Genomics (pymatgen): A robust, open-source python library for materials analysis. *Comput. Mater. Sci.* **2013**, *68*, 314−319.
(43) Patridge, C. J.; Love, C. T.; Swider-Lyons, K. E.; Twigg, M. E.; Ramaker, D. E. In-situ X-ray absorption spectroscopy analysis of capacity fade in nanoscale-$LiCoO_2$. *J. Solid State Chem.* **2013**, *203*, 134−144.
(44) Ichihara, F.; Niitsu, K.; Tanaka, Y.; Niwa, Y.; Mitsuishi, K.; Miyoshi, S.; Ohno, T.; Masuda, T. Structural Analysis of the $LiCoPO_4$ Electrode/NASICON-Type $Li_{1.3}Al_{0.3}Ti_{1.7}(PO_4)_3$ Solid Electrolyte Interface. *J. Phys. Chem. C* **2023**, *127* (31), 15043−15050.
(45) Antolini, E.; Ferretti, M. Synthesis and Thermal Stability of $LiCoO_2$. *J. Solid State Chem.* **1995**, *117* (1), 1−7.
(46) Waetzig, K.; Rost, A.; Heubner, C.; Coeler, M.; Nikolowski, K.; Wolter, M.; Schilm, J. Synthesis and sintering of $Li_{1.3}Al_{0.3}Ti_{1.7}(PO_4)_3$ (LATP) electrolyte for ceramics with improved Li^+ conductivity. *J. Alloys Compd.* **2020**, *818*, 153237.
(47) Picard, J. P.; Baud, G.; Besse, J. P.; Chevalier, R. Croissance cristalline et étude structurale de Co_3O_4. *J. Less-Common Met.* **1980**, *75* (1), 99−104.
(48) Hirota, K.; Inoue, T.; Mochida, N.; Ohtsuka, A. Study of Germanium Spinels (Part 3). *J. Ceram. Soc. Jpn.* **1990**, *98* (1141), 976−986.
(49) Dalton, M.; Gameson, I.; Armstrong, A. R.; Edwards, P. P. Structure of the $Li_{1+x}Ti_{2-x}O_4$ superconducting system: A neutron diffraction study. *Phys. C* **1994**, *221* (1), 149−156.
(50) Gummow, R. J.; Liles, D. C.; Thackeray, M. M. Spinel versus layered structures for lithium cobalt oxide synthesised at 400°C. *Mater. Res. Bull.* **1993**, *28* (3), 235−246.
(51) Mouhib, Y.; Belaiche, M.; Ferdi, C. A.; Lacham, M.; Elacham, A. New technique for elaboration and characterization of a high voltage spinel $LiCo_2O_4$ cathode and theoretical investigation. *New J. Chem.* **2020**, *44* (6), 2538−2546.
(52) Jovic, N.; Antic, B.; Kremenovic, A.; Spasojevic-de Bire, A.; Spasojevic, V. Cation ordering and order−disorder phase transitionin Co-substituted $Li_4Ti_5O_{12}$ spinels. *Phys. Status Solidi A* **2003**, *198* (1), 18−28.
(53) Wu, X.; Scott, K. A Li-doped Co_3O_4 oxygen evolution catalyst for non-precious metal alkaline anion exchange membrane water electrolysers. *Int. J. Hydrogen Energy* **2013**, *38* (8), 3123−3129.
(54) Liu, H.; Jin, S.; Zhang, K.; Jiang, Y.; Feng, Y.; Li, D.; Tang, P. Tuning the sensing selectivity of mesoporous hierarchical Ti-doped Co_3O_4 to toluene and xylene via controlling the oxygen defects. *Appl. Surf. Sci.* **2023**, *614*, 156079.
(55) Miranda-López, M. I.; Padilla-Zarate, E. A.; Hernández, M. B.; Falcón-Franco, L. A.; García-Villarreal, S.; García-Quiñonez, L. V.; Zambrano-Robledo, P.; Toxqui-Terán, A.; Aguilar-Martínez, J. A. Comparison between the use of Co_3O_4 or CoO on microstructure and electrical properties in a varistor system based on SnO_2. *J. Alloys Compd.* **2020**, *824*, 153952.
(56) Tang, C.-W.; Wang, C.-B.; Chien, S.-H. Characterization of cobalt oxides studied by FT-IR, Raman, TPR and TG-MS. *Thermochim. Acta* **2008**, *473* (1), 68−73.
(57) Brežný, B.; Muan, A. Phase relations and stabilities of compounds in the system $CoO{\bullet}TiO_2$. *J. Inorg. Nucl. Chem.* **1969**, *31* (3), 649−655.
(58) Anderson, K. P.; Giri, A. K.; Vinci, R. P.; Chan, H. M. Single crystal growth of $CoTi_2O_5$ by solid state reaction synthesis. *J. Am. Ceram. Soc.* **2019**, *102* (9), 5050−5062.
(59) Han, S.-W.; Jeong, J.; Yoon, D.-H. Effects of high-energy milling on the solid-state synthesis of pure nano-sized $Li_4Ti_5O_{12}$ for high power lithium battery applications. *Appl. Phys. A: Mater. Sci. Process.* **2014**, *114* (3), 925−930.
(60) Yu, Z.; Sun, Y.; Gong, H.; Shen, B. The effects of raw materials particle sizes on the solid-state reaction progress, morphology and magnetic properties of M-type strontium hexaferrites. *Ceram. Int.* **2024**, *50* (22), 46062−46068.

https://doi.org/10.1021/acs.jpcc.5c02329
J. Phys. Chem. C 2025, 129, 12738−12749